

# Poglavje 1

## Povzetek doktorskega dela

### 1.1 Uvod

Fizika delcev je eden od stebrov fizike, z močnimi koreninami, ki segajo vse do začetka 20. stoletja. Natančni eksperimenti in preverljiva teorija so pokazali, da vesolje sestoji iz osnovnih delcev in nosilcev interakcij. Osnovne delce delimo na kvarke ( $u, d, s, c, b, t$ ) in leptone, ki so nadaljnje razdeljeni na nabite leptone ( $e, \mu, \tau$ ) in pa nevtrine ( $\nu_e, \nu_\mu, \nu_\tau$ ). Nosilci treh (od štirih) osnovnih interakcij, s katerimi se ukvarjamo na tem področju, so fotoni ( $\gamma$ ) za elektromagnetno, gluoni ( $g$ ) za močno in nabiti- ( $W^\pm$ ) ter nevtralni ( $Z^0$ ) bozoni za šibko interakcijo. Vsi delci in njihovi zrcalni partnerji, antidelci (označeni z  $\bar{\phantom{x}}$ ), imajo maso, ki jim jo določa Higgsov bozon ( $H$ ). Vse delce ter interakcije med njimi opisuje Standardni model, ki je osrednja teorije fizike visokih energij. Kvarke lahko združujemo v kombinacije oblike  $q_1 q_2 q_3$  (hadroni) ali pa  $q_1 \bar{q}_2$  (mezoni), med katere sodijo tudi protoni in nevtroni, ki jih opazimo v naravi. Poleg omenjenih dolgo-živečih delcev pa obstajajo tudi težji, manj stabilni delci, ki preko zgoraj naštetih interakcij razpadejo v lažje, stabilnejše. Raziskovanje takšnih procesov s pomočjo pospeševalnikov in trkalnikov nam omogoča spoznavanje zakonov vesolja danes pa vse do njegovega začetka.

Osrednji del doktorske disertacije predstavljajo meritve razpadov mezonov  $B$ , delcev, ki so sestavljeni iz težkega kvarka  $b$  in enega od lahkkih kvarkov  $u$  ali  $d$ . Ena bolj presegajočih lastnosti vesolja je kršitev simetrije  $CP$ , t.j. kombinacije simetrij konjugacije naboja ( $C$ ) in prostorske inverzije ( $P$ ). Simetrija  $CP$  nakazuje, da so fizikalni procesi delcev in zrcalni procesi antidelcev enaki, kar pa danes vemo, da ne drži v celoti in poznamo procese, ki to simetrijo kršijo. Kršitev simetrije  $CP$  je tesno povezana s šibko interakcijo, to pa predstavlja našo motivacijo za študijo mezonov  $B$ , saj šibki razpadi predstavljajo večji del vseh razpadov mezonov  $B$ .

Edinstvena lastnost šibke interakcije je, da lahko spreminja tip oziroma t.i. okus kvarkov, medtem ko ga ostale interakcije ohranjajo. Takšni procesi so opisani s prehodno matriko

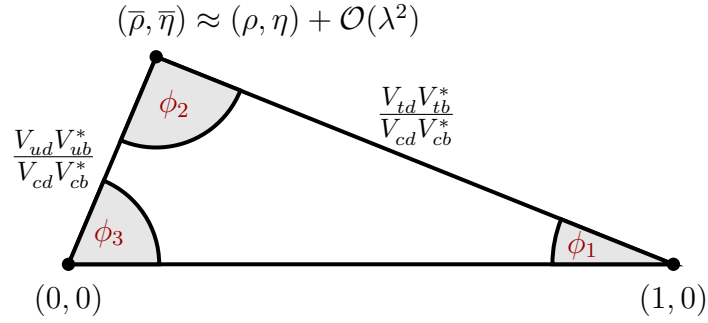
27 CKM (Cabibbo-Kobayashi-Maskawa) [1, 2]

$$V_{CKM} = \begin{bmatrix} V_{ud} & V_{us} & V_{ub} \\ V_{cd} & V_{cs} & V_{cb} \\ V_{td} & V_{ts} & V_{tb} \end{bmatrix}. \quad (1.1)$$

28 Unitarnost matrike CKM nam omogoča, da iz nje izluščimo matematične identitete, od  
29 katerih je ena pomembnejših

$$V_{ud}V_{ub}^* + V_{cd}V_{cb}^* + V_{td}V_{tb}^* = 0, \quad (1.2)$$

30 poznana pod imenom unitarni trikotnik, saj predstavlja zaključen vektor treh točk v  
31 kompleksni ravnini, kot prikazuje Slika 1.1. Parametri matrike CKM niso določljivi  
32 s strani teorije, temveč jih moramo določiti z eksperimentalnimi meritvami tako, da  
33 najdemo procese, ki so tesno povezani s stranicami in koti unitarnega trikotnika. Na  
34 tak način lahko preverimo, če je oblika trikotnika konsistentna, kar predstavlja dober  
35 test Standardnega modela, oziroma če so potencialno prisotni kakšni novi procesi, ki  
36 jih še ne poznamo, in jih kolektivno imenujemo "nova fizika". Dodatna motivacija za  
37 študijo mezonov  $B$  je ta, da velik delež njihovih razpadov predstavlja koristne procese  
38 za meritev unitarnega trikotnika.



Slika 1.1: Unitarni trikotnik s parametri  $\lambda$ ,  $\eta$ ,  $\rho$  and  $A$  (slednji ni prikazan), ki predstavlja proste parametre matrike CKM.

39 Procesi, ki jih študiramo v tej analizi, so tesno povezani z elementom  $V_{ub}$  matrike CKM,  
40 saj le-ta opisuje prehode kvarkov  $b \rightarrow c$ . Od vseh elementov, je absolutna vrednost  
41 tega elementa najmanjša, relativna napaka pa največja, zato meritve iz tega področja  
42 potencialno omogočajo največ izboljšave. Takšni prehodi kvarkov so prisotni v nearobnih  
43 (t.j. brez kvarkov  $c$ ) semi-leptonskih razpadih mezonov  $B$  oblike

$$B^+ \rightarrow X_u^0 \ell^+ \nu_\ell, \quad (1.3)$$

44 kjer  $X_u^0$  predstavlja nečarnobne mezone,  $\ell$  pa je eden od nabitih leptonov. Frekvenco  
45 razpadov, ki je tesno povezana z elementom  $V_{ub}$ , opišemo z enačbo

$$d\Gamma \propto G_F^2 |V_{ub}|^2 |L^\mu \langle X_u | \bar{u} \gamma_\mu \frac{1}{2} (1 - \gamma_5) b | B \rangle|^2, \quad (1.4)$$

46 kjer  $G_F$  predstavlja Fermijevo konstanto,  $L^\mu$  leptonski tok, izraz v Diracovih oklepajih  
 47 pa hadronski tok. V takšnih prehodih  $|V_{ub}|^2$  predstavlja verjetnost za prehod  $b \rightarrow u$ .

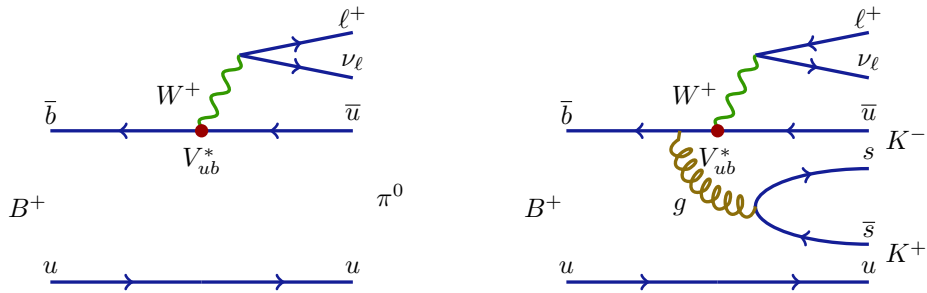
Meritev elementa  $V_{ub}$  je možna na ekskluziven in inkluziven način, kjer pri prvi metodi opravljamo meritve v specifično definirana končna stanja, kot na primer  $B \rightarrow \pi \ell \nu$ , pri drugi metodi pa opravljamo meritev s kupno končno stanje oblike  $B \rightarrow X_u \ell \nu$ . Obe metodi potekata preko različnih pristopov in se soočata z različnimi težavami, kar pomeni, da sta oba končna rezultata nekorelirana. Rezultata obeh meritev imata tudi zelo podobno natančnost, medtem ko se srednja vrednost le deloma ujema. Rezultata se razlikujeta s signifikanco  $3\sigma$ , kar predstavlja večjo težavo znotraj področja. Trenutni svetovni povprečji [3] ekskluzivne (iz razpadov  $B^0 \rightarrow \pi^- \ell^+ \nu$ ) in inkluzivne meritve (GGOU kolaboracija [4]) sta

$$|V_{ub}|_{\text{e.}} = (3.65 \pm 0.09 \pm 0.11) \times 10^{-3}, \quad (1.5)$$

$$|V_{ub}|_{\text{i.}}^{\text{GGOU}} = (4.52 \pm 0.15 \pm_{-0.14}^{+0.11}) \times 10^{-3}, \quad (1.6)$$

48 kjer prva in druga napaka predstavljata eksperimentalno in teoretsko napako. Rezultati  
 49 inkluzivnih meritev so praviloma večji kot rezultati ekskluzivnih. Razlogov za neujema-  
 50 nje je lahko več, od nepoznanih napak pri eksperimentu ali teoriji, do prispevkov nove  
 51 fizike.

52 V tej analizi se osredotočamo na enega od možnih razlogov za zgoraj omenjeno neujema-  
 53 nje, konkretnije za razpad  $B^+ \rightarrow K^+ K^- \ell^+ \nu$ , ki je strukturno precej podoben razpadu  
 54  $B \rightarrow \pi \ell \nu$  za razliko produkcije para kvarkov  $s\bar{s}$  ki se potem hadronizira v nove delce, kot  
 55 prikazuje Slika 1.2. V inkluzivnih meritvah nečarobnih semi-leptonskih razpadov me-  
 56 zonov  $B$  se standardno uporablja  $K$ -veto, t.j. selekcija, kjer zahtevamo, da v končnem  
 57 stanju nimamo mezonov  $K$  (sestava  $q\bar{s}$ ,  $q \in [u, d]$ ), poznanih tudi pod imenom kaoni.  
 58 Kaoni v končnem stanju nakazujejo na pogost prehod kvarkov  $b \rightarrow c \rightarrow s$ , ki pa jih  
 59 hočemo v analizah prehodov  $b \rightarrow u$  zatreti. V primeru naše analize imamo v končnem  
 60 stanju 2 kaona s preходом  $b \rightarrow u$ , kar pomeni, da takšni razpadi niso upoštevani v  
 61 inkluzivnih meritvah, čeprav bi morali biti. Cilj študije je določiti pogostost razpadov  
 62  $B^+ \rightarrow K^+ K^- \ell^+ \nu$  s preходом  $b \rightarrow u$  in s tem oceniti, kakšen potencialen efekt ima  
 63 lahko neupoštevanje teh razpadov na inkluzivno meritev elementa  $V_{ub}$ . V nadaljevanju  
 64 bo razpad  $B^+ \rightarrow K^+ K^- \ell^+ \nu$  zaradi enostavnosti zapisan kot  $B \rightarrow K K \ell \nu$ .



Slika 1.2: Feynmanovi diagrami za razpada  $B^+ \rightarrow \pi^0 \ell^+ \nu_\ell$  (levo) in  $B^+ \rightarrow K^- K^+ \ell^+ \nu_\ell$  (desno).

## 1.2 Experimentalna postavitve

Podatki, uporabljeni v tej analizi, so bili ustvarjeni pri trkih elektronov  $e^-$  in pozitronov  $e^+$  v pospeevalniku KEKB in zajeti z detektorjem Belle. Eksperiment je trajal od leta 1999 do 2010 pod okriljem znanstvene organizacije KEK v mestu Tsukuba na Japonskem. Trki delcev so se dogajali pri energiji, ki je ustrezala masi resonance  $\Upsilon(4S)$ , (sestava  $b\bar{b}$ ). V tem delu disertacije sta opisana pospeevalnik in detektor, podrobnejši opis pa se nahaja v literaturah [5] in [6].

### 1.2.1 Trkalnik KEKB

KEKB je asimetričen trkalnik delcev  $e^+e^-$ , ki potujejo po obroih s premerom 3 km v gruah. V središču detektorja grui elektronov z energijo 8 GeV in pozitronov z energijo 3.5 GeV trita pod kotom 22 mrad. Skupna invariantna masa trka ustreza masi resonance  $\Upsilon(4S)$

$$E_{CM} = 2\sqrt{E_{e^+}E_{e^-}} = m_{\Upsilon(4S)}c^2 \approx 10.58 \text{ GeV}. \quad (1.7)$$

Dele mezonov  $\Upsilon(4S)$  razpade preko zelo istega kanala v dva praktino mirujoča mezona  $B$ , kar tej in v podobnih analizah pogosto izkoriamo, saj je začetno stanje dobro poznano.

Trkalnik je v asu obratovanja zajel količino podatkov, ki ustreza integrirani luminoznosti  $1041 \text{ fb}^{-1}$ , od katere okoli  $711 \text{ fb}^{-1}$  predstavlja podatke, zajete pri energiji 10.58 GeV, t.j. masi resonance  $\Upsilon(4S)$ . Slednja vrednost integrirane luminoznosti ustreza številu  $771 \times 10^6$  parov  $B\bar{B}$  mezonov.

### 1.2.2 Detektor Belle

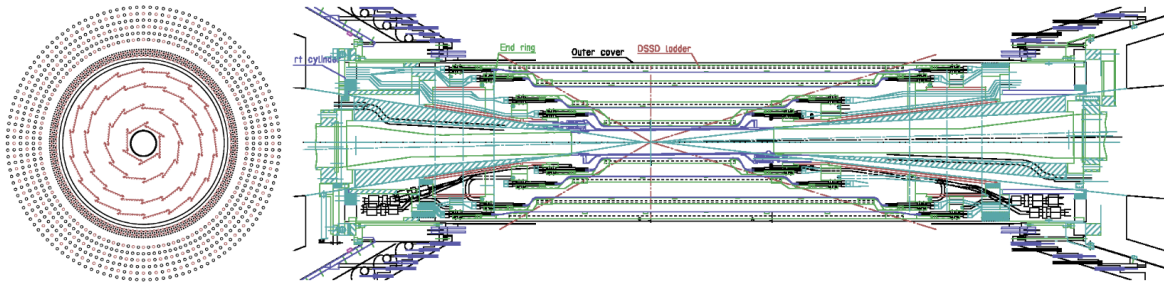
The Belle detector is a magnetic mass spectrometer which covers a large solid angle. It is designed to detect remnants of  $e^+e^-$  collisions. The detector is configured around a 1.5 T superconducting solenoid and iron structure surrounding the interaction point (IP). The 4-momentum of the decaying  $B$  mesons and its decayed daughter particles are determined via a series of sub-detector systems, which are installed in an onion-like shape. Short-lived particle decay vertices are measured by the silicon vertex detector (SVD) situated outside of a cylindrical beryllium beam pipe. Long-lived charged particle momentum is measured via tracking, which is performed by a wire drift chamber (CDC). Particle identification is provided by energy-loss measurements in CDC, aerogel Cherenkov counters (ACC) and time-of-flight counters (TOF), situated radially outside of CDC. Particles producing electromagnetic showers deposit energy in an array of CsI(Tl) crystals, known as the electromagnetic calorimeter (ECL), which is located inside the solenoid coil. Muons and  $K_L$  mesons (KLM) are identified by arrays of resistive plate counters in the iron yoke on the outside of the coil.

The coordinate system of the Belle detector originates at the IP, with the  $z$  axis pointing in the opposite direction of the positron beam, the  $x$  axis pointing horizontally out of the ring, and the  $y$  axis being perpendicular to the aforementioned axes. The electron beam crosses the positron beam at an angle of about  $22^\circ$ . The polar angle  $\theta$  covers the region between  $17^\circ \leq \theta \leq 150^\circ$ , while the cylindrical angle  $\varphi$  covers the full  $360^\circ$  range, amounting to about 92% coverage of the full solid angle.

## Silicon Vertex Detector

SVD is the inner-most part of the Belle detector and serves the purpose of measuring the decay vertices of decaying particles. The precision of the subsystem is about  $100 \mu\text{m}$ , which is important for measuring the difference in  $z$ -vertex positions of the  $B$  mesons in time-dependent CP violation studies. The main part of the SVD are the double-sided silicon detectors (DSSD). With their thin profile and parallel silicon strips on both sides they provide 2D hit information of charged particle and are perfect for a small-scale device which acts with high precision.

During the data taking period, two configurations were of the SVD have been used. The first, SVD1, has three layers of DSSD detectors, positioned at 30, 45.5 and 60 mm away from the IP. They compose a ladder-like structure, covering the polar angle of  $23^\circ < \theta < 140^\circ$ . This configuration was used from the beginning of the experiment until 2003, when a dataset of about  $1.52 \times 10^8$  pairs of  $B\bar{B}$  mesons were recorded. Due to problems with radiation hardness, a new configuration was used, SVD2, which was operational until the end of data taking, measuring about  $6.20 \times 10^8$  pairs of  $B\bar{B}$  mesons. The SVD2 has 4 layers of DSSD detectors positioned at 20, 43.5, 70 and 80 mm away from the IP and covered the polar angle of  $17^\circ < \theta < 150^\circ$ . The first layer was moved closer to the IP, which greatly improved the sub-system precision, due to multiple-Coulomb scattering affecting resolution more as the distance from the IP increases. The front and side view of the SVD2 are shown in Figure 1.3.



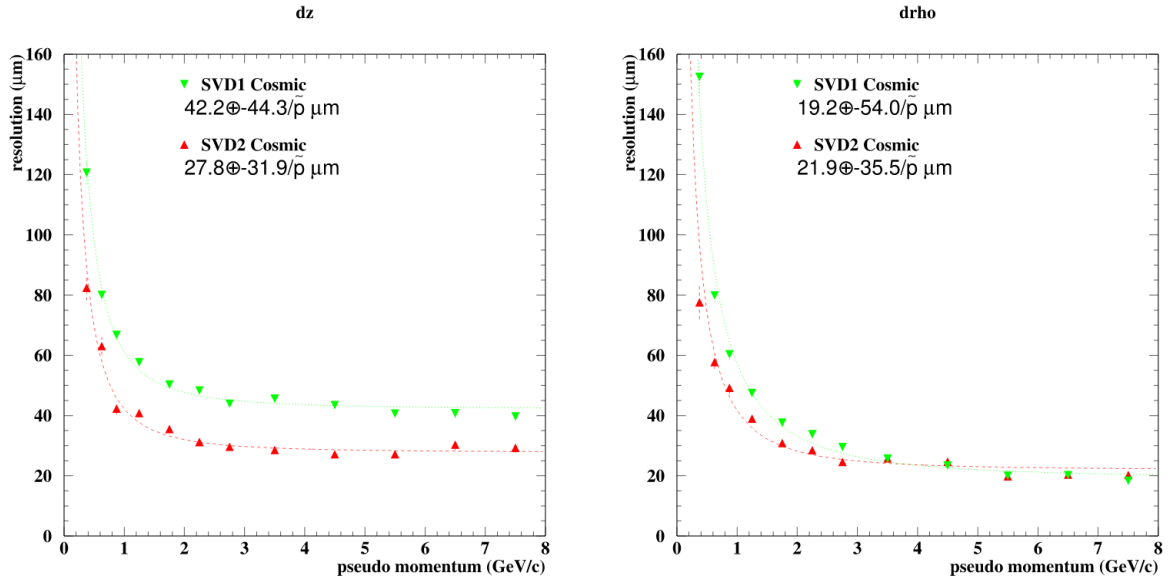
Slika 1.3: Front (left) and side (right) view of the SVD detector with the SVD2 configuration. The front view also shows the inner wires of the Drift Chamber [7].

The efficiency of the SVD was determined as a fraction of CDC tracks within the SVD acceptance that have associated SVD hits, needed for the  $B$  meson reconstruction. The average efficiency is found to be around 98% and is in agreement with simulation. SVD performance is also determined via the impact parameter  $z$  and  $r\phi$  resolution, which was obtained from cosmic ray data. The momentum and angular dependence of the impact parameters is shown in Figure 1.4 and is well represented by the following parametrization for the SVD2

$$\sigma_z = 28 \mu\text{m} \oplus \frac{32 \mu\text{m}}{(p/(1 \text{ GeV}/c)) \beta \sin^{5/2} \theta}, \quad (1.8)$$

$$\sigma_{r\phi} = 22 \mu\text{m} \oplus \frac{36 \mu\text{m}}{(p/(1 \text{ GeV}/c)) \beta \sin^{3/2} \theta}, \quad (1.9)$$

where  $p$  is the particle momentum,  $\theta$  is the polar angle, and  $\beta = v/c$ . An advantage of the smaller distance between the IP and the first DSSD layer in SVD2 is clearly seen.

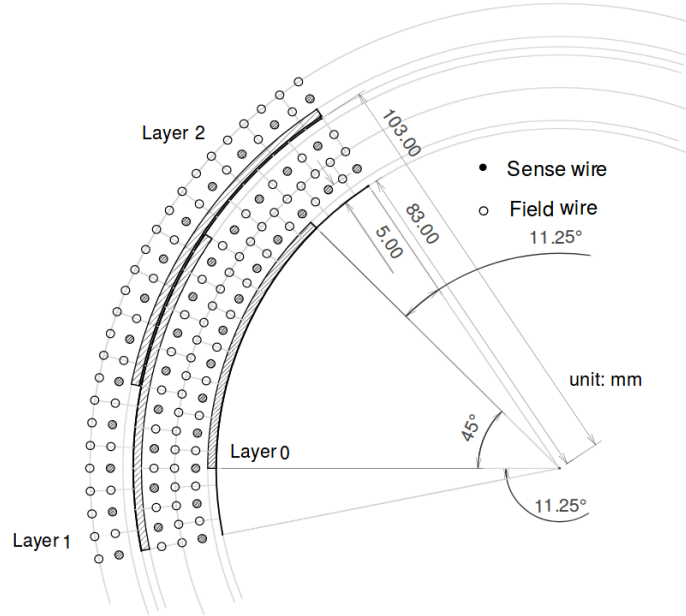


Slika 1.4: Impact parameter resolutions of  $z$  (left) and  $r\phi$  (right) coordinates for the SVD1 and SVD2 configuration of the vertex detector [7].

## Central Drift Chamber

CDC is a large-volume tracking device located at the central part of the Belle detector and is crucial for measurements of the particle trajectories and momenta, but also serves as a particle identification device (PID). It has a cylindrical structure with a radius of 88 cm, length of 2.4 m and acceptance equal to the one of SVD2. The chamber has a total of 8400 wires, which are positioned in 50 layers and describe a nearly square wire

configuration. There are two types of wires – field wires for producing the electrical field, and sense wires for detecting the particles. Odd-numbered wire layers are oriented in the  $z$  direction and provide measurement of the transverse momentum  $p_t$ , while even-numbered wires are inclined with respect to the  $z$  axis by a small angle of  $\pm 50$  mrad to allow for measuring of the polar angle of the track. The wire configuration is shown in Figure 1.5. The space between the wires is filled with a gas mixture of 1 : 1 helium-ethane, a low- $Z$  gas in order to minimize multiple-Coulomb scattering contributions to momentum resolution, since the majority of particles in  $B$  events have a momentum lower than 1 GeV/ $c$ . It also has a small cross section of the photoelectric effect, which is important to reduce background electrons induced by the synchrotron radiation from the beam.

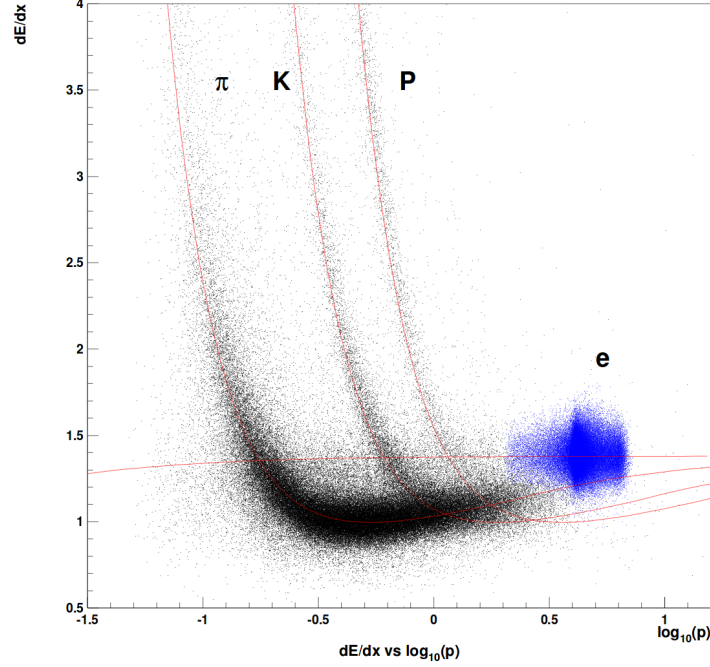


Slika 1.5: Cell structure of CDC [6].

Charged particles which pass the CDC wire frame cause gas ionization. The produced electrons drift toward the sense wires with great acceleration due to the strong electric field close to the wire. The accelerated electrons collide with gas molecules and produce secondary, tertiary etc. ionizations, which result in an electron avalanche, a process which increases the signal by many orders of magnitude. The primary electrons also have a specific drift velocity, which allows us to relate the measured pulse height and drift time to the energy deposit of the particle as well as the distance from the sense wire. This information is important for calculating the energy loss  $dE/dx$ .  $dE/dx$  as a function of momentum differs for different particles, as shown in Figure 1.6. This allows for identification purposes of, specifically for kaons and pions. In the momentum region less than 0.8 GeV/ $c$ ,  $dE/dx$  enables a separation between kaons and pions up to  $3\sigma$ . The resolution of the transverse momentum measurement with the CDC is a function

155 of the transverse momentum itself, as well as the particle velocity, and is parametrized  
 156 as

$$\sigma(p_T)/p_T = \frac{0.201\% p_T}{1 \text{ GeV}/c} \oplus \frac{0.290\%}{\beta}. \quad (1.10)$$



Slika 1.6: Measured  $dE/dx$  as a function of particle momentum. The red lines show the expected distribution for different types of particles [6].

## 157 Time-of-Flight Counter

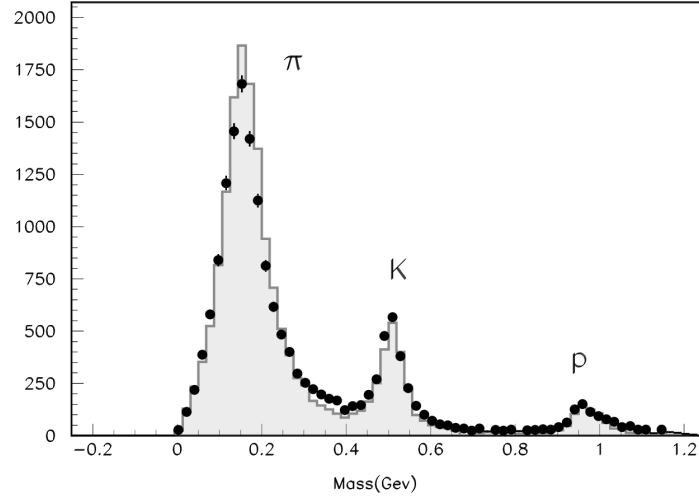
158 The purpose of the TOF subdetector is particle identification in the momentum region  
 159  $0.8 \text{ GeV}/c < p < 1.2 \text{ GeV}/c$ , especially for kaons and pions. There are 64 TOF modules  
 160 in the barrel region, covering the polar angle of  $33^\circ < \theta < 121^\circ$ . One TOF module  
 161 consists of two long polyvinyltoluene-based plastic scintillator bars, 4 fine-mesh photo-  
 162 multiplier tubes (PMT) at the 4 ends of the bars, and a trigger scintillation counter,  
 163 where the latter provides additional trigger information. TOF measures the time interval  
 164 between the  $e^+e^-$  collision and the passage of the particle through it. The mass of a  
 165 particle can be inferred via the relation

$$m^2 = \left( \frac{1}{\beta^2} - 1 \right) p^2 = \left( \frac{T^2 c^2}{L^2} - 1 \right) p^2, \quad (1.11)$$

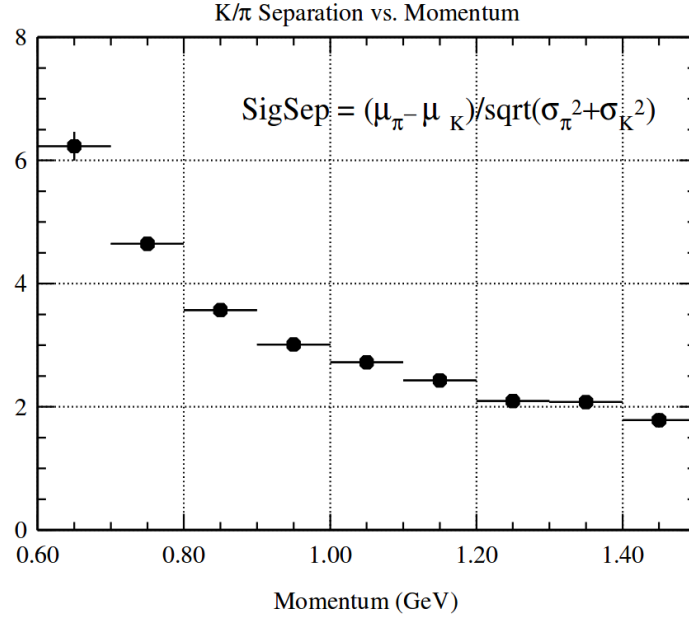
166 where  $T$  is the measured time interval,  $L$  is the charged particle trajectory length from  
 167 the IP to TOF and  $p$  is the charged particle momentum, determined by SVD and CDC.



168 The resulting mass distribution for charged tracks measured by TOF in hadron events  
 169 is shown in Figure 1.7, where clear peaks corresponding to pions, kaons and protons  
 170 can be seen. To achieve the good discrimination between kaons and pions, a time-of-  
 171 flight resolution of less than 100 ps is needed for particles with momentum below about  
 172 1.2 GeV/ $c$ , which encompasses 90% of the particles produced in  $\Upsilon(4S)$  decays. The  
 173 identification power can also be determined in the form of  $\pi^\pm/K^\pm$  separation significance  
 174 as a function of particle momentum, shown in Figure 1.8. A clear separation of about  
 175  $2\sigma$  is achieved for particle momenta up to 1.25 GeV/ $c$ .



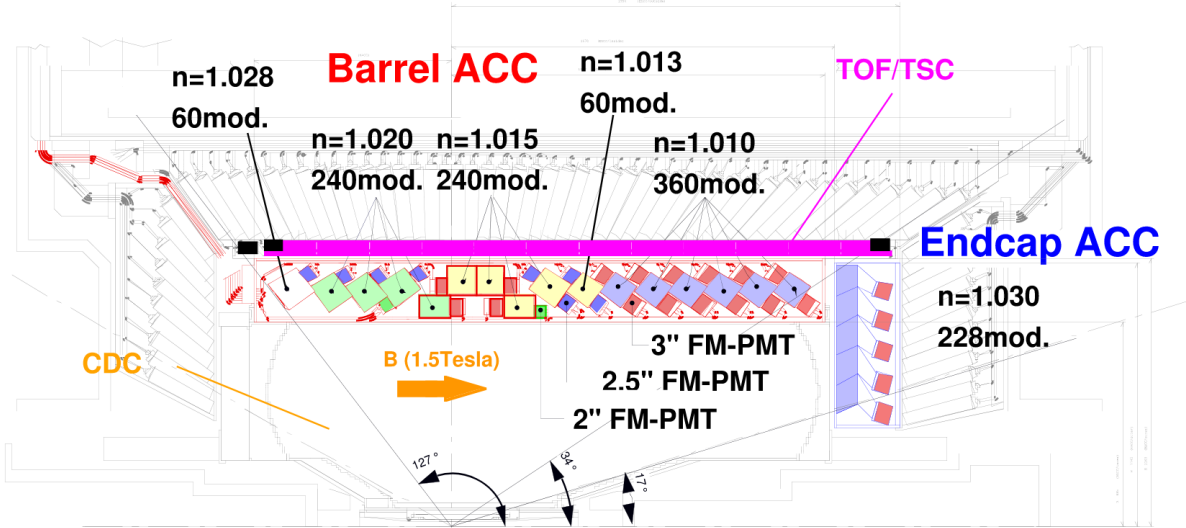
Slika 1.7: Mass distribution from TOF measurements for particle momenta below 1.2 GeV/ $c$  [6].



Slika 1.8:  $\pi^\pm/K^\pm$  separation by TOF [6].

## 176 Aerogel Cherenkov Counter

177 TOF is not capable of performing good PID above 1.2 GeV/c momentum, since  $\beta$  is  
 178 almost equal to 1. For higher momenta in the region 1.0 GeV/c < 4.0 GeV/c, the ACC  
 179 is introduced. It is a threshold-type Cherenkov counter which utilizes the fact that  
 180 particles emit Cherenkov light if the particle speed is greater than the speed of light in  
 181 the passing medium. ACC is introduced in the barrel region with 960 separate modules,  
 182 covering a polar angle of  $34^\circ < \theta < 127^\circ$  and 228 modules in the forward end-cap region,  
 183 with the polar angle coverage of  $17^\circ < \theta < 34^\circ$ . Each ACC module consists of an  
 184 aluminum encased block of silica aerogel and one or two fine-mesh PMTs encased on  
 185 each block to detect Cherenkov light pulses. Due to the polar angle dependence of the  
 186 particle momentum, 6 different refractive indices are chosen for the aerogel material,  
 187 ranging from 1.010 up to 1.030 and are controlled within 3% precision. The layout of  
 188 the ACC is shown in Figure 1.9.

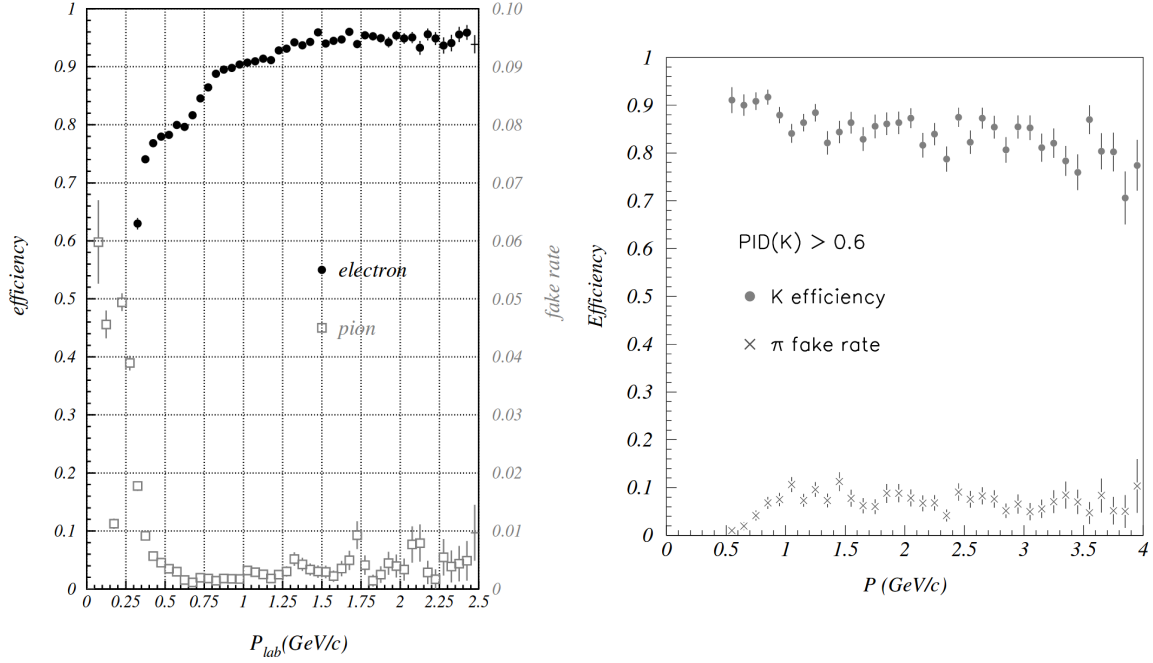


Slika 1.9: Cross-sectional view of the CDC (inner most), ACC and TOF (outer most) detectors [6].

189 The threshold velocity  $\beta$  of a given particle for Cherenkov radiation is

$$\beta \leq \frac{1}{n}, \quad (1.12)$$

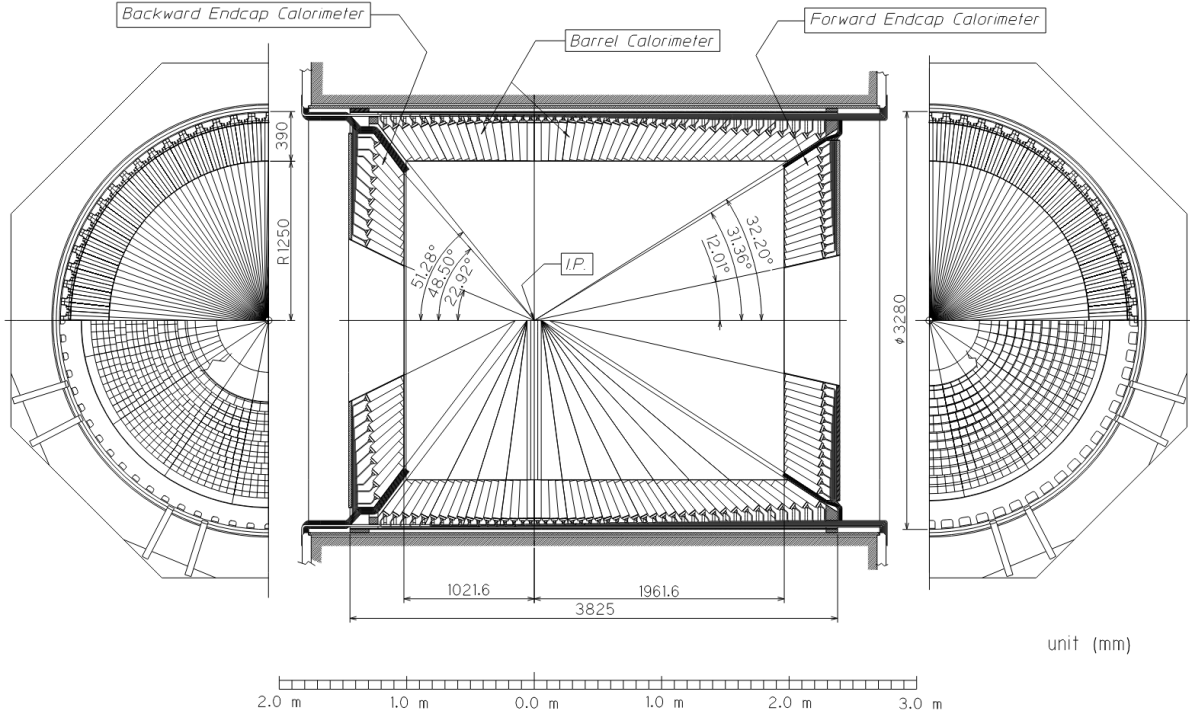
190 where  $n$  is the refractive index of the medium. The refractive indices in the ACC are  
 191 such that, due to different masses, pions will emit Cherenkov light and kaons will not,  
 192 due to different masses of the particles. Using the PID of ACC, along with other sub-  
 193 system PID info, the electron identification efficiency in the momentum range above  
 194 1 GeV/ $c$  is equal to or above 90% while the pion fake rate, the probability of wrongly  
 195 identifying pions as electrons, to be around 0.2 - 0.3%. Similarly for kaons, kaon ID  
 196 efficiency is equal to 80% for most of the momentum region up to 4 GeV/ $c$ , while pion  
 197 fake rate remains below 10%. Figure 1.10 shows the electron and kaon efficiencies and  
 198 the corresponding pion fake rates as a function of particle momenta.



Slika 1.10: Electron identification efficiency and fake rate for charged pions (left) and similarly for kaons (right). Note the different scales for the electron efficiency and fake rate in the former case [6].

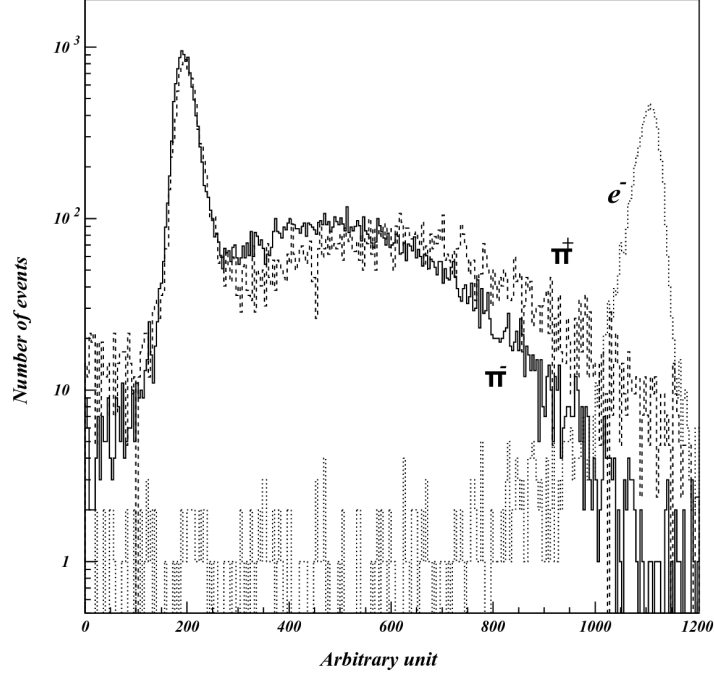
## Electromagnetic Calorimeter

Measurement of position and energy deposit of particles is performed in the ECL, especially for electrons and photons, where the latter are not measured by any of the subsystems described so far. It also provides complimentary particle identifications for electrons versus pions. The calorimeter consists of a highly segmented array of thallium-doped caesium iodide (CsI(Tl)) in the form of tower-shaped crystals, each pointing towards the IP. Each crystal is about 30 cm long with a width from 44.5 mm to 65 mm in the barrel, and from 44.5 mm to 82 mm in the end-caps. Out of a total of 8736 crystals with a total mass of about 43 tons, 6624 of them are positioned in the barrel region and 1152 (960) in the forward (backward) end-caps. The inner radius of the barrel section is about 1.25 m, while the end-caps are positioned at  $-1.0$  m and  $2.0$  m from the IP in direction of the  $z$  axis. The polar angle coverage of the barrel region is  $32.2^\circ < \theta < 128.7^\circ$ , and for the end-caps  $12.4^\circ < \theta < 31.4^\circ$  and  $130.7^\circ < \theta < 155.1^\circ$ . Figure 1.11 shows the layout of the barrel and end-caps ECL.



Slika 1.11: Overall configuration of the ECL [6].

213 When an electron or a photon hits a crystal, it produces an electromagnetic shower,  
 214 a result of the bremsstrahlung and pair-production effects. Heavier charged particles  
 215 do not interact in the same way and deposit only a small amount of energy by ioniza-  
 216 tion effects. The information from the ECL, compared with momentum measurements  
 217 provided by the CDC, enables the identification of electrons. The distribution of the  
 218 deposited energy for different particles is shown in Figure 1.12. The probability of mi-  
 219 sidentifying an electron as a pion is approximately 5% for momenta less than 1 GeV/ $c$ ,  
 220 and less than 1% for momenta above 2 GeV/ $c$ .



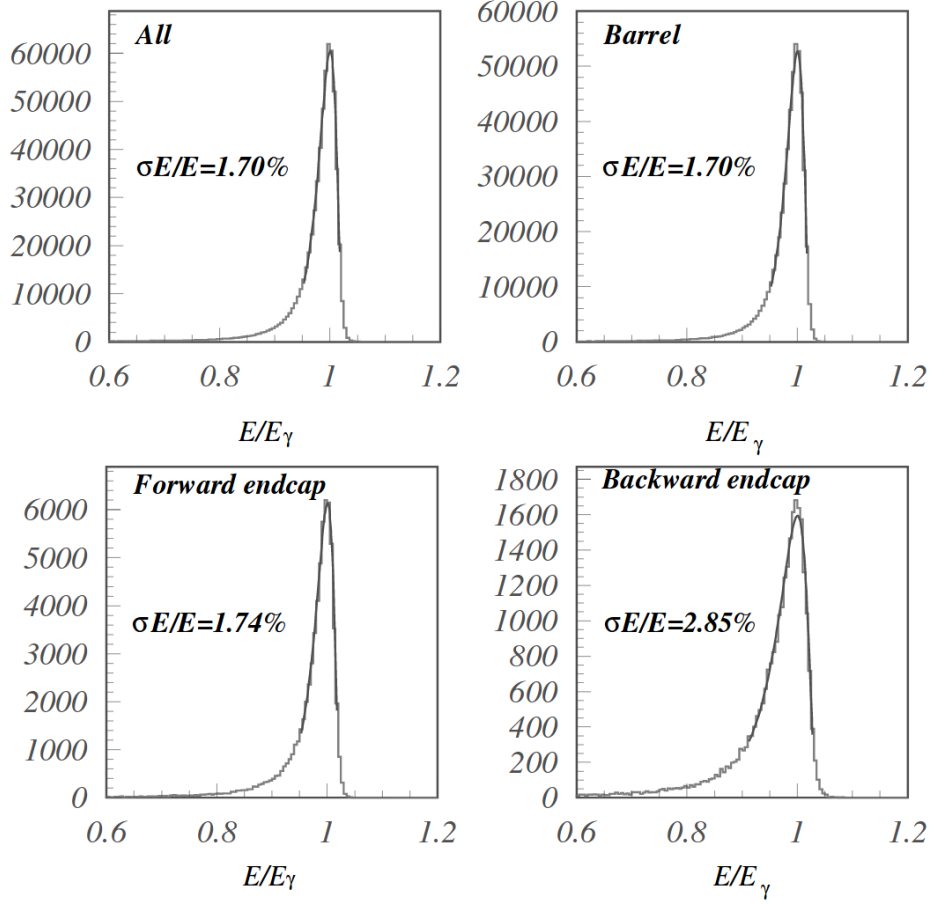
Slika 1.12: Distribution of the energy deposit by electrons and charged pions at 1 GeV/ $c$  momentum [6].

For ECL calibration,  $e^+e^- \rightarrow e^+e^-$  and  $e^+e^- \rightarrow \gamma\gamma$  events were used. The average energy resolution was achieved to be 1.7% for the barrel ECL, and 1.74% and 2.85% for the forward and backward ECL, respectively, as shown in Figure 1.13. These value are in good agreement with Monte Carlo predictions. Worse energy resolution in backward end-cap is due to the lower photon energy, which results in larger effects of passive material in front of the calorimeter [7]. The energy resolution as a function of energy can be obtained via the following relation

$$\frac{\sigma_E}{E} = \frac{0.0066\%}{(E/1 \text{ GeV})} \oplus \frac{1.53\%}{(E/1 \text{ GeV})^{1/4}} \oplus 1.18\%, \quad (1.13)$$

while the resolution of the position measurement is

$$\sigma_{pos} = 0.27 \text{ mm} + \frac{3.4 \text{ mm}}{(E/1 \text{ GeV})^{1/2}} + \frac{1.8 \text{ mm}}{(E/1 \text{ GeV})^{1/4}}. \quad (1.14)$$

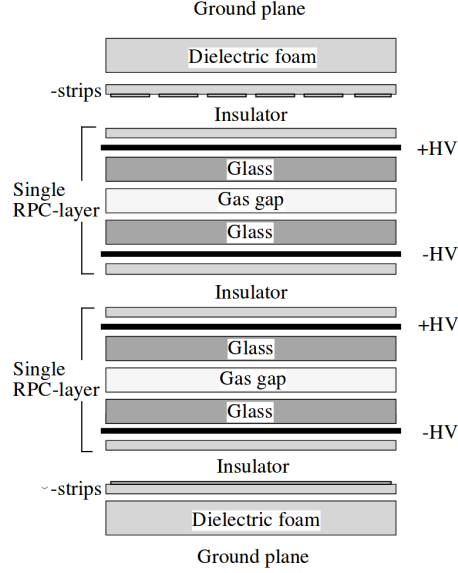


Slika 1.13: Reconstructed energy distribution for  $e^+e^- \rightarrow \gamma\gamma$  events for overall, barrel, forward and backward end-cap calorimeters [6].

## 229 $K_L^0/\mu$ Detector

230 The KLM detector is used for detection of high-penetration particles such as  $K_L^0$  and  $\mu$   
 231 for momenta larger than 0.6 GeV/c. The setup covers the polar angle of  $20^\circ < \theta < 155^\circ$ .  
 232 Detection of  $K_L^0$  particles is troublesome, since they are neutral and have a small material  
 233 interaction probability, therefore a lot of material is needed in the KLM. To provide  
 234 detection of both kinds of particles, hadronic and neutral, as well as electromagnetically  
 235 and hadronically interacting, the KLM is constructed as a sampling calorimeter, which  
 236 consists of 15 layers of 3.7 cm thick resistive-plate counters (RPC) with 14 layers of  
 237 4.7 cm thick iron plates between them. A single RPC module consists of two parallel  
 238 plate electrodes, two glass panels, and gas in between. A charged particle passing the  
 239 gas gap initiates a local discharge of the plates, which in turn induces signal to record the  
 240 time and location of ionization. This is possible since the resistivity of the glass surface  
 241 is high, so the discharge occurs locally. Hadrons interacting with the iron plates may

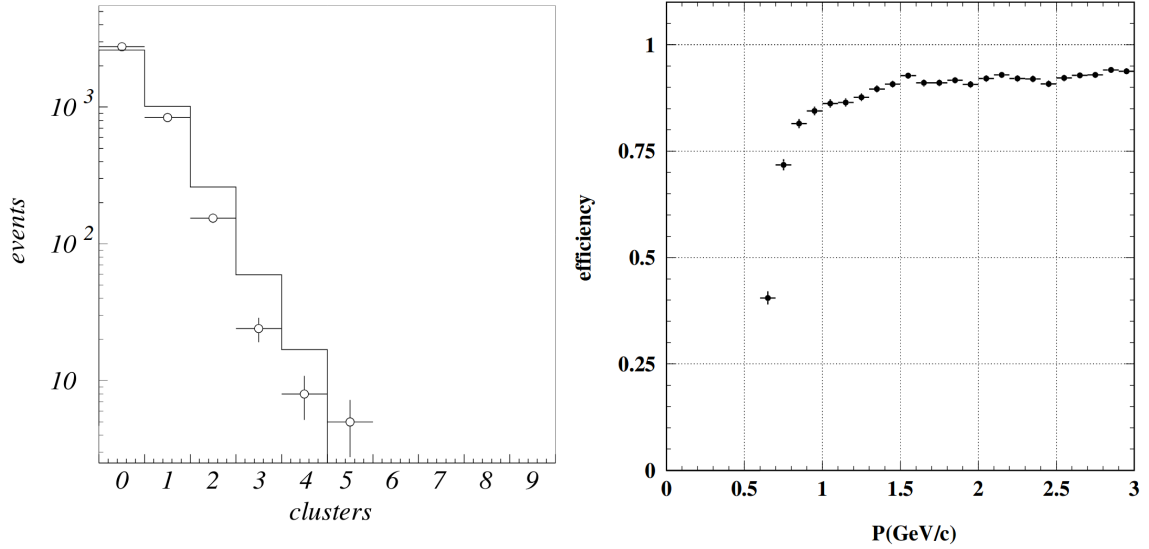
242 produce a shower of ionizing particles, which are then also detected by the RPCs. The  
 243 KLM is located outside of superconducting solenoid and the iron plates of the KLM serve  
 244 a dual role as the flux return for the magnetic field. Figure 1.14 shows a cross-section  
 245 of an RPC superlayer, consisting of an RPC pair.



Slika 1.14: Cross-section of an RPC superlayer, consisting of an RPC pair [6].

246 The  $K_L^0$  particle can be distinguished from other charged hadrons because they have  
 247 no matched track in the CDC. The flight direction can also be inferred from the hit  
 248 locations in the consecutive RPCs. Tracks of charged particles measured in CDC are  
 249 extrapolated into KLM and clusters within  $15^\circ$  of an extrapolated charged particle track  
 250 are excluded from  $K_L^0$  cluster candidates. On the other hand, muons with matched CDC  
 251 tracks are able to reach the KLM if their momentum is larger than  $0.5 \text{ GeV}/c$ . They  
 252 do not interact strongly and do not produce hadronic showers in the KLM, which serves  
 253 as a handle on the muon identification. Figure 1.15 (left) shows the number of neutral  
 254 clusters per event and a Monte Carlo simulation of the predicted number of  $K_L^0$  clusters  
 255 per event. The average number of  $K_L^0$  clusters per event is 0.5. The agreement with  
 256 the prediction gives us the confidence that the detector and our reconstruction software  
 257 are performing correctly. Figure 1.15 (right) shows the muon detection efficiency as a  
 258 function of momentum and shown for a likelihood cut of 0.66, where muon likelihood is  
 259 based on the comparison of the measured range of a particle with the predicted range  
 260 for a muon. Based on  $K_S \rightarrow \pi^+\pi^-$  events, a muon identification efficiency of better than  
 261 90% is determined, with a pion fake rate of less than 5% for particles with momenta  
 262 more than  $1.5 \text{ GeV}/c$  and a likelihood cut of 0.66.





Slika 1.15: Number of neutral clusters per event in KLM (left) and muon detection efficiency as a function of momentum in KLM (right) [6].

Cosmic ray events have been used to determine efficiency and resolution of the KLM, with an overall efficiency typically over 98%. The temporal and spatial resolution of the KLM are few ns and about 1.2 cm, respectively. The latter corresponds to an angular resolution from the interaction point of better than 10 mrad.

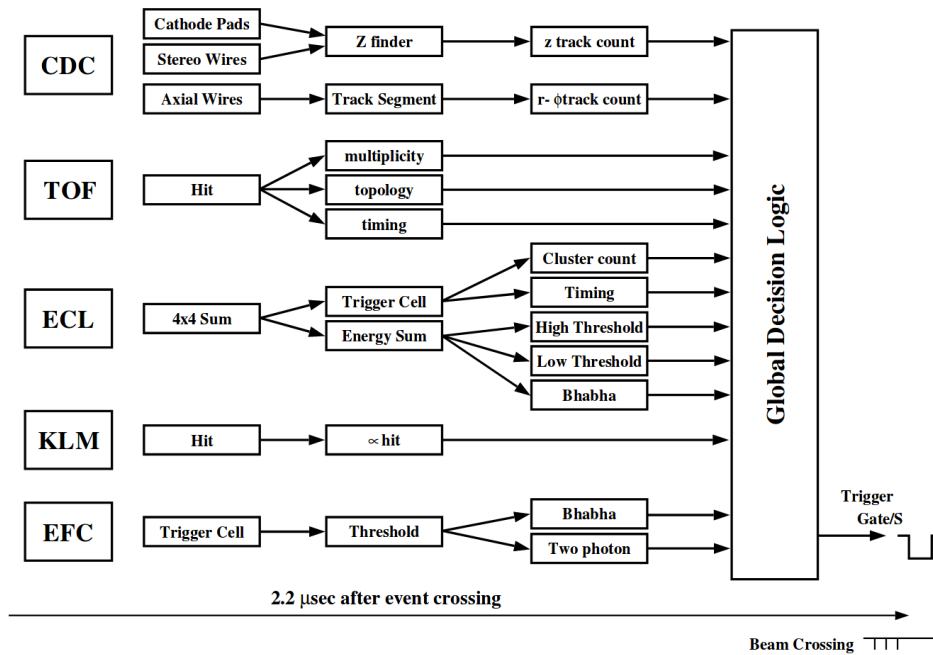
In order to to detector calibration and proper luminosity measurements, we need to accumulate samples of Bhabha and  $\gamma\gamma$  scattering. Otherwise, as shown in Table ??, the cross-section for physics events of interest is reasonably small. During normal operation (luminosity of  $L = 10 \times 10^{34} \text{ cm}^{-2}\text{s}^{-1}$ ) the total event rate is around 200 Hz, which is well below the data acquisition (DAQ) limit of 500 Hz. Out of this rate, 100 Hz are physically interesting events, which include also two photon events, Bhabha scattering and  $\mu$  pair production, besides hadronic events from  $B\bar{B}$  pair events. In order to discard events which are not interesting for physics analyses, we use a trigger system by appropriately applying restrictive conditions. This section describes the necessary procedures and equipment to successfully do so.

## Trigger System

The trigger system operates by immediately eliminating events that are not of interest, so that the amount of stored data is within the 500 Hz frequency limit, while the efficiency for physics events of interest is kept high. Events which pass the triggers are then stored, otherwise discarded. The Belle trigger system consists of three stages, Level-1 (L1) online hardware trigger, Level-3 (L3) online software trigger and Level-4 (L4) offline

software trigger.

L1 trigger is the first stage of the trigger system, which consists of multiple sub-detector triggers, all connected to a central trigger system called the Global Decision Logic (GDL), as schematically shown in Figure 1.16. Each sub-detector trigger works on a principle of either a track trigger or an energy trigger. In the former case the triggers discard events not meeting conditions based on the number of reconstructed tracks or track hits, while the latter is based on the total energy deposit and counting of crystal hits. Each sub-detector processes the event information and provides it to the GDL, where all the information is combined and the current event is characterized. The information from the sub-detector triggers reaches the GDL within  $1.85 \mu\text{s}$  after the collision, and the final trigger signal is provided within at a fixed  $2.2 \mu\text{s}$  latency. The combined efficiency from the L1 trigger is greater than 99.5% for hadronic events.



Slika 1.16: The Level-1 trigger system for the Belle detector [6].

After passing L1 trigger, the L3 discards background events from the software-wise perspective. L3 is an online software trigger which performs a simple, but fast reconstruction of the event. Events with at least one track satisfying the impact parameter condition  $|dz| < 5.0 \text{ cm}$  and with a total energy deposit in the ECL more than  $1 \text{ GeV}/c$  are selected. The L3 trigger reduces the event rate by 50%, with a 99% efficiency for hadronic events.

After passing the L3 trigger, the events are recorded on tapes. However, these data still contain many events from the beam background. To reduce the background events even

303 further, they are required to pass the L4 offline software filtering. At the same time, high  
304 efficiencies for signal events is still required. Events must satisfy the following conditions

- 305     • have at least one track with  $p_T > 300$  MeV/ $c$  and impact parameters  $|dr| < 1.0$  cm  
306       and  $|dz| < 4.0$  cm,
- 307     • have total energy deposit in the ECL must greater than 4 GeV.

308 Approximately 27% of triggered events are passed through L4, while keeping an almost  
309 full efficiency for hadronic events. Events that pass the L4 trigger are fully reconstructed  
310 and stored to the DST. Overall, the efficiency of hadronic events after all trigger stages  
311 is measured to be more than 99%, which is more than the requirements from physics  
312 analyses.

### 313 **1.3 Postopek analize**

### 314 **1.4 Sistematske negotovosti**

### 315 **1.5 Končni rezultat**